Available online at www.sciencedirect.com

SciVerse ScienceDirect

Ceramics International 39 (2013) 4437–4448

CERAMICS INTERNATIONAL

www.elsevier.com/locate/ceramint

Influence of original powders on the microstructure and properties of thermal barrier coatings deposited by supersonic atmospheric plasma spraying, part II: Properties

Y. Bai[a,b], L. Zhao[a], J.J. Tang[a], S.Q. Ma[a], C.H. Ding[c], J.F. Yang[a], L. Yu[b], Z.H. Han[a,*]

[a]State Key Laboratory for Mechanical Behavior of Materials, Xi'an Jiaotong University, Xi'an 710049, PR China
[b]School of Mechanical Engineering, Xi'an Jiaotong University, Xi'an 710049, PR China
[c]State Key Laboratory for Strength and Vibration of Mechanical Structures, Xi'an Jiaotong University, Xi'an 710049, PR China

Received 7 September 2012; received in revised form 6 November 2012; accepted 13 November 2012
Available online 23 November 2012

Abstract

In this paper, the thermal shock resistance, oxidation resistance and thermal insulation performance of "conventional" microsized and nanostructured coatings (named as MC and NC respectively) deposited by supersonic atmospheric plasma spraying (SAPS) were investigated. The results showed that due to the improvement of intersplat cohesion and bonding strength between the top coat and bond coat, the MC presented a higher thermal shock resistance, which was distinct from the previous reports about the property difference between the conventional and nanostructured coatings. In addition, the result from isothermal oxidation test indicated that the oxidation kinetics of both coatings followed a parabolic law. The weight gain of MC was slightly lower than that of NC before 600 h at 1100 °C. However, due to the formation of vertical cracks which penetrated the whole top coat, the weight gain for MC after 1000 h was slightly higher than that of NC, indicating that the NC had a higher oxidation resistance after long time exposure. Meantime, because lots of fine cracks were formed between the unmelted particles and lamellar structures, the temperature drop (ΔT) of NC increased with the increase of testing times. The nanostructured SAPS-coating showed better oxidation resistance and thermal insulation properties, but the inter-splat cohesion and top coat/ bond coat interface adhesion are still needed to be improved in order to increase its thermal cycling life.

Keywords: C. Thermal shock resistance; Oxidation resistance; Thermal insulation property; Supersonic atmospheric plasma spraying

1. Introduction

Thermal barrier coatings (TBCs) have been widely applied to protect the hot-section components of modern gas turbine engine from the extremely aggressive environments [1]. The TBC typically consists of a ceramic Y_2O_3 partially stabilised ZrO_2 (YSZ) top coat and a metallic bond coat, usually MCrAlY, where M is usually nickel, cobalt, or combination of these two. The bond coat enhances the adhesion and provides a good thermal expansion match between the top coat and the substrate. In addition, during high-temperature service, oxidation of the bond coat can lead to the formation of thermally grown oxides (TGOs) at the original top coat/bond coat interface.

Among the thermo-mechanical properties of TBCs related to the high temperature application, the thermal shock resistance, oxidation resistance and thermal insulation capacity are of central importance. TBCs have a tendency to spall or debond under thermal cycling conditions at high temperature. It was found that the failure of TBCs during the thermal cycles was associated with the spallation of the ceramic coat due to the buildup of thermal stresses, which generated by the temperature gradients in service, ceramic sintering, phase transformation, corrosive and erosive attack and residual stresses arising from the deposition process [2,3]. In addition, during high temperature exposure or thermal cycling,

*Corresponding author. Tel.: +86 2982668614; fax: +86 29 82663453.
E-mail address: zhhan@mail.xjtu.edu.cn (Z.H. Han).

0272-8842/$ - see front matter © 2012 Elsevier Ltd and Techna Group S.r.l. All rights reserved.
http://dx.doi.org/10.1016/j.ceramint.2012.11.037

cracks initiated and propagated within or close to the TGO layer as the result of oxidation of bond coat at high-temperature exposure. These large delamination cracks can finally cause the spallation of the top ceramic coat and failure of TBC system. Due to the porous and micro-cracked structure of plasma sprayed coatings, some studies considered that the top ceramic coat was transparent to oxygen penetration [4,5]. However, some studies have suggested that the presence of the top coat can reduce the oxidation rate of bond coat to some extent [6,7]. Therefore, the effect of composition and microstructure of top coat on the oxidation behavior of bond coat is needed to be further investigated.

The thermal insulation property of TBCs is usually evaluated by thermal conductivity, which had a close relationship with the microstructure of coating. The plasma sprayed TBCs exhibited typical layered and porous microstructures. The interlamellar boundaries or cracks running parallel to the ceramic/metal interface can effectively reduce the high-temperature thermal conductivity of coating. However, the above defects are considered as a source of weakness, which can result in the failure of TBC system since they leave the coating relatively less strain-tolerant [8]. Therefore, how to tailor the microstructure, which can provide a balance between low thermal conductivity and high thermal cycling life, is still a hot research topic in the field of TBCs.

In part I [9] of this two-part series, the microstructural difference between the microsized and nanosized coatings deposited by supersonic atmospheric plasma spraying (SAPS) was studied. In this part, the property difference between the above two types of coatings, including thermal shock resistance, oxidation resistance and thermal insulation property will be discussed in detail.

2. Experimental procedure

2.1. Bonding strength and thermal shock test

The bonding strength of the as-sprayed coatings was measured using a material tester (Instron1196, USA) in accordance with ASTM C 633-79 standard. A rod made of nickel-base superalloy, GH3030, was used as the substrate with a diameter of 25.4 mm. Film epoxy adhesive (FM-1000, USA) with tensile fracture strength more than 60 MPa was applied. The final value represented the average value of 5 samples sprayed at the same parameters. Thermal shock tests were conducted by using a muffle furnace. When the temperature inside the furnace reached to 1100 °C, the samples were pushed into the furnace. The holding time at the temperature was 5 min, then the samples were directly quenched into water, the temperature of the water throughout the cycling was between 20 and 30 °C. More than 10% of the spalled region of the surface of the top coating (quantitatively calculated by image analysis software Image Tool 3.0) was adopted as criteria for the failure of the coating.

2.2. Isothermal oxidation test and specimen characterization

The size of substrate (nickel-base superalloy) for isothermal oxidation test was 35 mm × 14 mm × 3 mm and all the surfaces of substrate were fully coated by TBCs. To characterize the oxidation behavior of samples, static oxidation experiments were carried out in a silicon carbide tube furnace under isothermal condition at 1100 °C. All the specimens were kept in alumina crucibles and inserted into the hot zone of the furnace during the test. After different exposure times, the weight change measurements were made with the help of an electronic balance with a sensitivity of 0.1 mg. Besides, the oxidized samples were sectioned after completion of a predetermined exposure time. Before specimen sectioning, the surface of top coat was coated by two-part thermosetting resin in order to protect the microstructure of samples from damage during cutting afterwards. After the resin was cured at 120 °C for 1 h, cross-sections were produced by wet diamond sawing at lower speed in order to minimize damage. One side was ground on 600-grit silicon carbide papers, followed by sequential polishing on soft cloths until no obvious scratches were observed by optical microscopy. The microstructure and phase compositions of samples were examined by TESCAN-VEGAII XUM scanning electron microscope (SEM) and X-ray diffraction (XRD, D/MAX-2400X, Rigaku, Japan) using Cu Kα radiation. The voltage and current setting were 40 kV and 100 mA, respectively. The range of scattering angle (2θ) was from 20° to 80°. Samples were continuously scanned with a stepsize of 0.02° (2θ) and a speed of 0.12° s^{-1}.

2.3. Thermal conductivity and thermal insulation test

Free-standing top YSZ coat samples with a diameter of 10.0 mm and a thickness of 1.0 mm were used for thermal diffusivity measurement (LFA 457 Micro Flash Analyzer, NETZSCH, Germany). The 1.0 mm thick YSZ samples were firstly deposited on the surface of metallic substrate and then separated from it by submerging the samples in 40% hydrochloric acid until the metallic substrate was fully dissolved. The laser-flash diffusivity method was used to explore the thermal diffusivity in the temperature range from 500 °C to 1100 °C. In order to assure complete absorption of the laser-flash at the sample surface and the measurement of the transient temperature at the opposite surface, the coating samples were coated with a carbon film before the measurement. The thermal conductivity of sample was calculated using the following equation:

$$k(T) = \alpha(T)\rho C_p(T) \quad (1)$$

where k stands for thermal conductivity, α is thermal diffusivity, C_p is heat capacity, and the density ρ of the coating was measured using Archimedes' principle. Density was assumed to be constant at all temperatures.

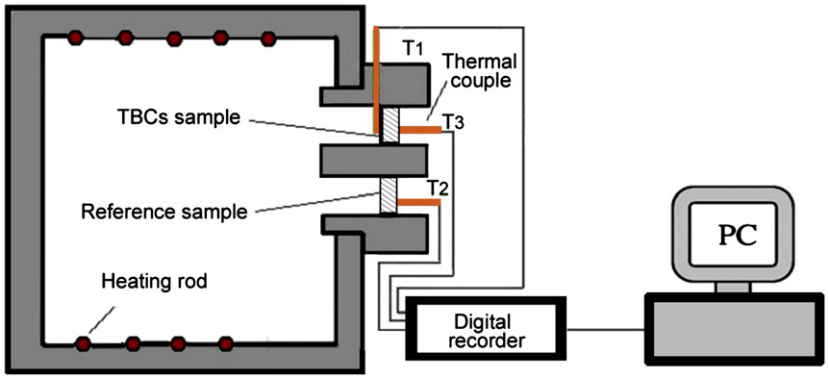

Fig. 1. Schematic of self-made experimental set-up used to evaluate the thermal insulation property of TBCs.

In addition, in order to directly evaluate the thermal insulation property of coatings, the thermal insulation test was carried out by a self-made experimental set-up as shown in Fig. 1. Thermocouple 1 was used to measure the front side temperature inside the electrical furnace near the YSZ-based TBCs. Thermocouple 2 was used to measure the temperature of the back side of a reference sample without TBCs outside the electrical furnace. Thermocouple 3 was used to measure the temperature of the back side of samples with TBCs outside the electrical furnace. The diameter and thickness of the reference sample were 25.4 mm and 3.2 mm, respectively. The sample with TBCs had the same shape, but the thickness was about 260 μm higher than that of the reference sample, because a bond coat (60 μm in thickness) and a YSZ top coat (200 μm in thickness) were deposited. The measured temperatures were named as T_1, T_2 and T_3, respectively, and could be automatically recorded. The temperature drop ($\Delta T = T_2 - T_3$) reflected the thermal insulation performance of SAPS-TBCs, and the higher the ΔT was, the better the thermal insulation property was. It was noted that the 1.0 mm thick freestanding YSZ samples were also placed near the thermocouple 1 in the furnace in order to obtain thermal conductivity of samples (after thermal insulation test) by laser-flash diffusivity method.

3. Results and discussion

3.1. Bonding strength and thermal shock test

According to ASTM C 633-79 standard, bonding strengths between top coat and bond coat of SAPS microsized coating (MC) and nanosized coating (NC) were 52 ± 4 and 47 ± 7 MPa, respectively. Previous investigations illustrated that the bonding strengths of nanosized and microsized coatings deposited by conventional atmospheric plasma spraying were 40 ± 5 MPa and 36 ± 3 MPa, respectively [10–12]. Therefore, the bonding strength of NC was slightly higher than that of APS nanostructured coating, whereas the bonding strength of MC was greatly improved compared with the APS conventional microsized coating. As stated in part I, the NC exhibited a multi-modal microstructure and the unmelted nano particles were loosely embedded in the well-flattened splats. These unmelted particles, on one hand, may improve the compliance of residual stress of TBCs in service [13]; on the other hand, it could decrease the effective bonding surface between splats and the underlying bond coat, leading to the decrease of bonding strength. The previous work from other researchers showed that the nanostructured coating had a higher bonding strength than that of conventional coating [10]. This can be explained by the fact that the conventional coating deposited by APS usually exhibited a porous and microcracked structure, resulting in weak bonding at the interface between the top coat and bond coat. However, due to the significant improvement of velocity and surface temperature of in-flight particles during the SAPS process, the coatings deposited by SAPS had a denser microstructure and the porosity was significantly reduced. Densities of MC and NC were 5.7 and 5.5 g cm^{-3} by using the Archimedes' principle in deionized water considering the theoretical density of YSZ coating was approximately 6.0 g cm^{-3} [14–16]. As described in part I, due to the lower particle size, the microsized feedstock powders would impinge onto the substrate surface and previously deposited layers with lower viscosity levels (higher degree of melting throughout the entire particle) compared with agglomerated nanosized powders. Consequently, the splat-to-splat cohesion may be better than that of the NC. Moreover, microhardness was defined as resistance to penetration and could indirectly reflect the splat-to-splat cohesion of thermal sprayed coatings. A higher hardness implied a greater degree of splat-to-splat cohesion [17]. The Vickers hardness of the NC was 704 ± 74 kg mm^{-2}, whereas MC was 820 ± 49 kg mm^{-2} measured 30 times on the polished cross section with a load of 300 g pressure and a holding time of 10 s. The above result also indicated that the splat-to-splat cohesion of the MC was higher than that of the NC.

Fig. 2 shows the surface morphology of MC and NC after different thermal cycles. As seen from Fig. 2(a), the evidently visible cracks on the fringe of MC was found after 300 cycles (noted by white arrows), and sustained up to 350 cycles, about 5% of surface area spalled, while

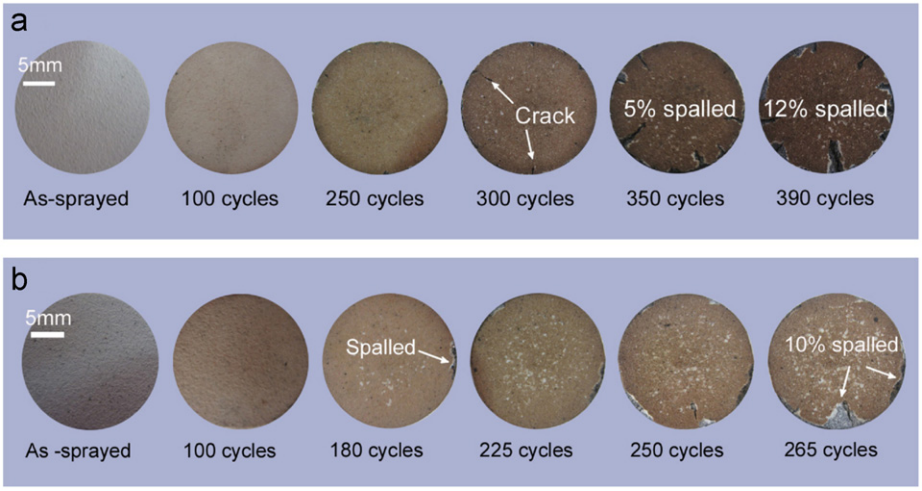

Fig. 2. Surface morphology of coatings after different thermal cycles: (a) MC and (b) NC.

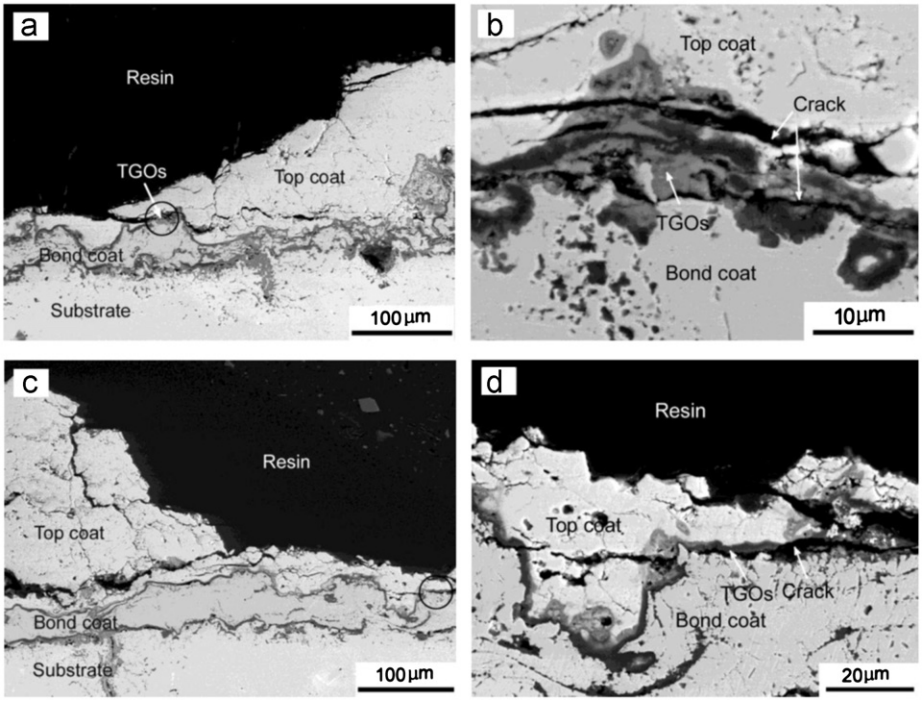

Fig. 3. SEM micrographs of coatings after different thermal cycles: (a) MC after 390 thermal cycles, (b) circular region of (a) observed at higher magnification, (c) NC after 265 thermal cycles, (d) circular region of (c) observed at higher magnification.

approximately 12% of surface area spalled after 390 cycles. For NC, as shown in Fig. 2(b), after 180 cycles, some white spots were found on the center of the sample, which may be attributed to a small mount of YSZ top coat delaminated and spalled from the surface of samples. In addition, obvious surface spallation of the coating, as noted by an arrow, was observed on the right edge of sample after 180 cycles and about 10% of surface area spalled after 265 cycles. Therefore, the thermal cycling life of MC was about 50% higher than that of NC. Due to the extreme heating and cooling conditions encountered at the edges, large-area spallation was found on the fringe of samples. Fig. 3 shows the spallation of top coat near the edges of MC and NC. As seen from Fig. 3a and b, after 390 thermal cycles, some coarse cracks (basically horizontal to the top coat/bond coat interface) formed at the splat–splat boundaries, top coat/TGO interface and inside of TGO in the MC. These cracks propagated to the inside of top coat leading to the spallation of top coat. Meanwhile, as shown in Fig. 3c and d, the NC had a similar failure mode with the MC and the spallation occurred above the top coat/TGO interface. The TGO was formed by oxidation of metallic bondcoat during the thermal cycles and predominantly comprised of alumina as well as some oxide clusters of chromia, nickel oxide and spinel phases [18]. Because the TGO was between the YSZ top coat and the metallic bond coat, excessive TGO growth

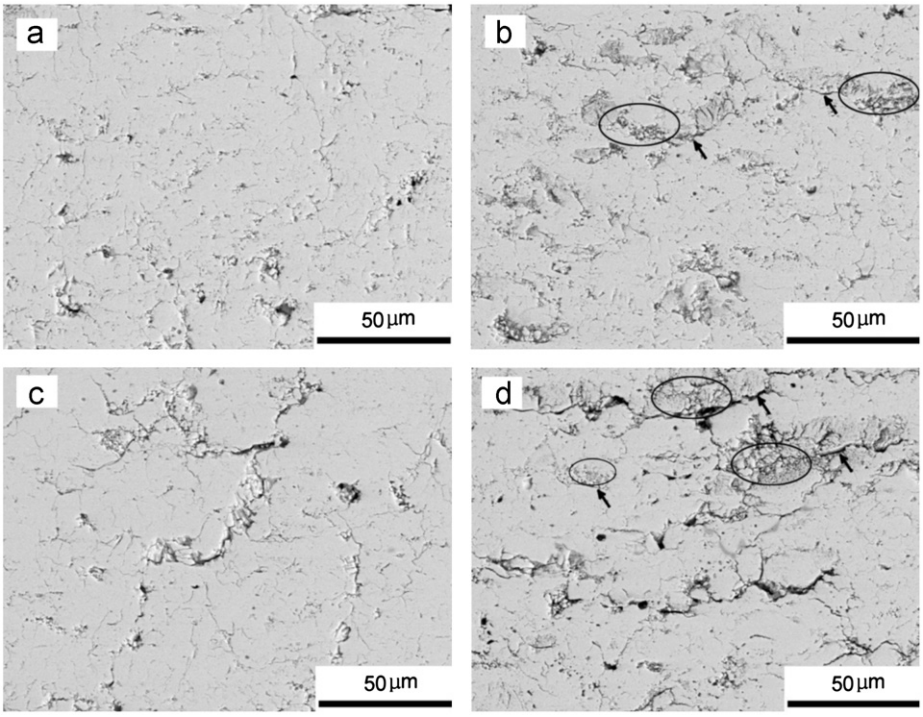

Fig. 4. SEM micrographs of central regions of coatings after different thermal cycles: (a) MC after 100 thermal cycles, (b) NC after 100 thermal cycles, the unmelted particles and cracks were denoted by black ellipses and arrows respectively, (c) MC after 390 thermal cycles, (d) NC after 265 thermal cycles, the unmelted particles and cracks were denoted by black ellipses and arrows respectively.

would increase the stress between the two layers, thus lead to the delamination of TBCs [18–21]. The above results demonstrated that the failure of MC and NC during thermal cycles was associated with the initiation and propagation of cracks at the splat boundaries, top coat/TGO interface and inside of TGO. The whole process was progressive and the damage progression was related to the extension of micro cracks followed by linking-up, and then the coarse cracks propagated until a large surface area of top YSZ coat spalled from the TBC system.

Fig. 4 shows SEM micrographs of central regions of coatings after different thermal cycles. As seen from Fig. 4a and b, many micro-cracks were found in both of the coatings after 100 thermal cycles. However, as shown in Fig. 4c and d, it was found that lots of coarse cracks with length of several tens of micrometers were formed in NC after 265 thermal cycles. These cracks were almost parallel to the top coat/bond coat interface and some of cracks were located at the boundary between unmelted particle and lamellar structure. Some works from other researchers showed that the unmelted particles distributed in the nanostructured coating could arrest the propagation of cracks and had a positive rule in improving the toughness of coating [22]. But it can be hypothesized that lamellar structures were disrupted by these unmelted particles and cracks tended to initiate and propagate along the splat boundaries owing to the weak intersplat bonding. Gell et al. pointed out that one simple mechanism could be used to describe the micro-debonding process concerned with the bonding strength degraded and the bonding stress increased after the engine experienced some thermal cycles, where the increased tensile stress met the reduced interface strength, localized debonding occurred [23]. Therefore, from the above results, it can be inferred that due to the enhanced intersplat cohesion and top coat/bond coat adhesion, the thermal shock resistance of MC was greatly improved compared with NC.

3.2. Isothermal oxidation kinetics

Fig. 5 shows isothermal oxidation kinetics of MC and NC at 1100 °C. As shown in Fig. 5(a), both of coatings showed a near-parabolic weight gain behavior and the weight gain was higher in the early stage of the oxidation since the selective oxidation occurred [24–26]. The weight gain of MC was slightly lower than that of NC before 600 h. However, the weight gain for MC after 1000 h was 6.8 mg cm^{-2}, slightly higher than 6.3 mg cm^{-2} of NC indicating the NC had a higher oxidation resistance after long time exposure at high temperature. The following formula was used to describe the oxidation kinetics as a function of oxidation time.

$$\Delta W = (K_p t)^n \tag{2}$$

where ΔW is the oxidation weight gain per unit surface area, K_p is the oxidation rate constant, t is the oxidation time, n is a constant. In this work, the values of n and K_p were calculated by the following linear fit:

$$\lg \Delta W = n(\lg k_p + \lg t) \tag{3}$$

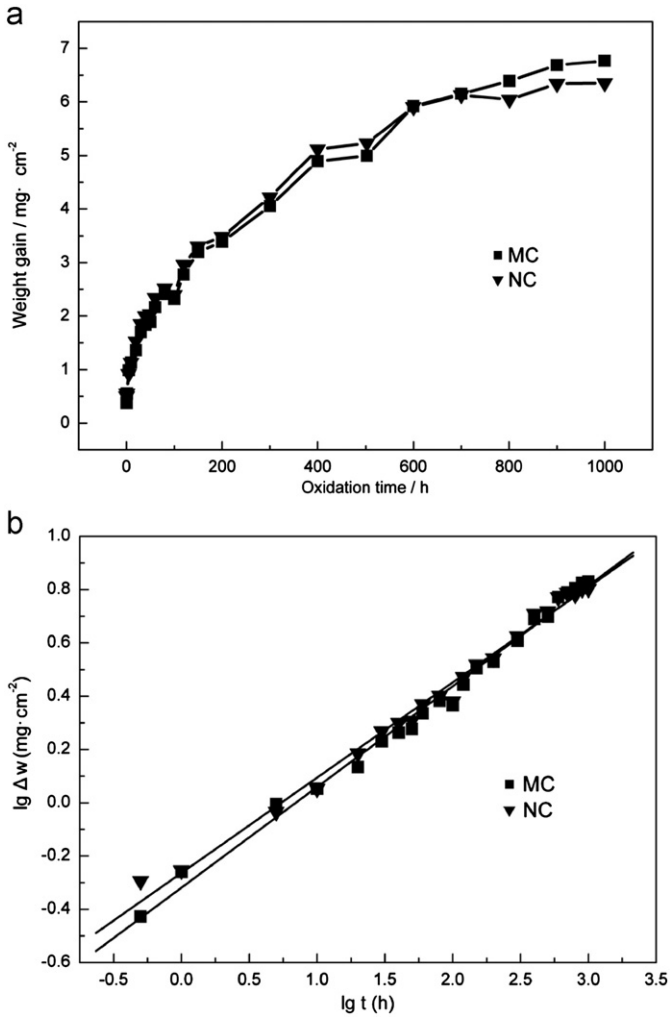

Fig. 5. Isothermal oxidation kinetics of MC and NC at 1100 °C: (a) weight gain per unit area as a function of oxidation time and (b) variation of logarithm of weight gain with logarithm of oxidation time.

Table 1
The values of n and K_p calculated by linear fit.

Samples	n	K_p ($(mg\ cm^{-2})^{1/h}\ h^{-1}$)
MC	0.38	0.14
NC	0.36	0.18

Fig. 5(b) shows the variation of $lg\Delta W$ against lgt for the MC and NC at 1100 °C. The slope of MC and NC were calculated as 0.38 and 0.36, respectively in the $lg\ \Delta W - lgt$ plot. The values of n and K_p are listed in Table 1. It is proposed that both permeation of O_2 and diffusion of O^{2-} ions contributes to the oxygen transportation through the top coat and causes the bond coat to oxidize [7]. The as-sprayed MC with lower porosity could effectively decrease the diffusive channels for oxygen and reduce the oxygen pressure at the top/bond coat interface, thus effectively hindering the delivery of oxygen into the bond coat and reducing the growth rate of TGO. On the other hand, the loosely distributed un-melted particles made it easier for the transport of oxygen ions in the NC. As a consequence, the weight gain of MC was slightly lower than that of NC at the initial stage of oxidation. As the oxidation proceeded, the microstructure of as-sprayed coating was changed. Fig. 6 shows the SEM micrographs of MC and NC after oxidation for 600 h at 1100 °C. As seen from Fig. 6(a), one coarse crack was found in the MC, which was perpendicular to the top coat/bond coat interface and penetrated the whole top YSZ coat. This type of penetrated crack was parallel to the heat flux and promoted the delivery of oxygen into the bond coat leading to a higher growth rate of TGO. In addition, although the top YSZ coat was not spalled from the TBC system, some cracks parallel to the top coat/bond coat interface were observed in MC, since the excessive TGO growth increased the stress between the top coat and bond coat. On the contrary, as shown in Fig. 6(b), some fine vertical cracks were found in

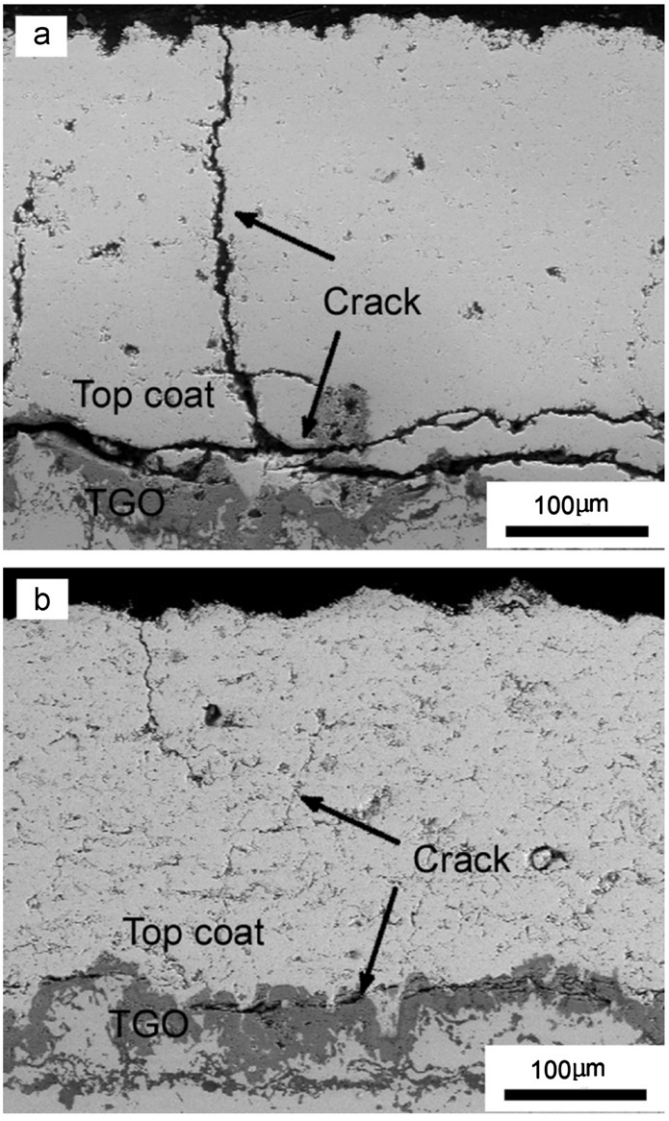

Fig. 6. SEM micrographs of coatings after 600 h oxidation at 1100 °C: (a) MC and (b) NC.

the NC coat after oxidation for 600 h. These fine cracks did not penetrate the whole top coat and stopped in the area above the top coat/bond coat interface. Hence, the formation of coarse vertical crack was the main reason for the higher weight gain of MC after 600 h as shown in Fig. 5(a).

The phase composition of coatings after 600 h oxidation was analyzed by X-ray diffraction. The XRD patterns of coatings are shown in Fig. 7. As observed from Fig. 7, both of the coatings were composed of a mixture of non-transformable tetragonal t′ and tetragonal *t* zirconia phases, as illustrated in high-angle region (72–76°) of the diffraction (see Fig. 7b) [27]. In addition, no monoclinic phase was observed, as illustrated in low-angle region (28–32°) of the diffraction (see Fig. 7c). If the tetragonal phase transformed to monoclinic phase after long-term exposure at high temperature, large amounts of stress would be generated due to the about 3–4% volume increase, which may lead to the formation of cracks [28]. Based on the above analysis, it can be concluded that the phase transformation stress was not the driving force for the formation of vertical cracks in MC. The in-plane tensile stress may be one reason to explain the formation of vertical crack. The in-plane tensile stresses can be generated as a result of thermal expansion mismatch between the ceramic top coat and the metallic substrate. The higher thermal expansion coefficient of the substrate ensured that the top coat was under significant tension at the high temperature. Meanwhile, owing to the increased rate of diffusional processes at high temperature, sintering could apparently start leading to the shrinkage of the deposited splats and reduction of volume of YSZ top coat. The accumulated sintering strains may provide the driving force for the vertical crack [29,30]. For the conventional porous YSZ coating, the shrinkage strain may be absorbed or compensated by the porosity, which can prevent the formation of vertical cracks. However, the MC deposited by SAPS had a denser microstructure and higher splat–splat cohesion, thus the vertical-crack tendency was more obvious.

3.3. Thermal insulation property

The fundamental function of TBCs is to decrease the temperature of metal substrate. Therefore, thermal insulation property is considered as one of the most important factors to evaluate the performance of TBCs. In this work, the thermal insulation performance of TBCs was evaluated by the temperature drop across TBCs ($\Delta T = T_2 - T_3$) in a self-made set-up. Fig. 8a and b show the recorded heating temperature curves of furnace (T_1), reference specimen backside (T_2) and TBCs specimen backside (T_3) after different test times. As shown in Fig. 8a and b, T_2 and T_3 increased with increasing furnace temperature T_1. Meanwhile, T_2 and T_3 gradually became stable when the holding time was longer than 2 h at 1100 °C. The temperature drops across TBCs (ΔT) measured at 1100 °C for 4 h are shown in Fig. 8(c). As observed from it, the temperature drops of as-sprayed MC and NC were 71 °C and 81 °C, respectively. The temperature drop of MC was

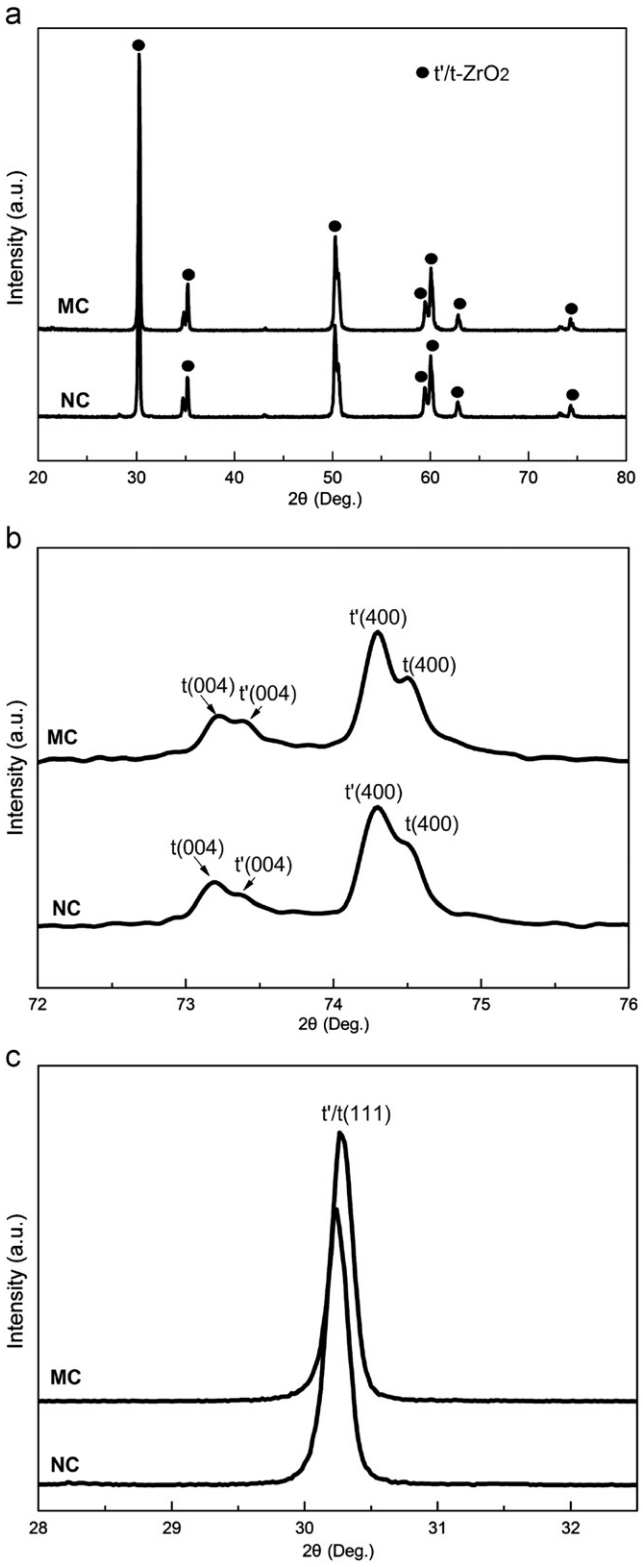

Fig. 7. XRD patterns of coatings after 600 h oxidation at 1100 °C: (a) the whole pattern, (b) high-angle region of the diffraction pattern and (c) low-angle region of the diffraction pattern.

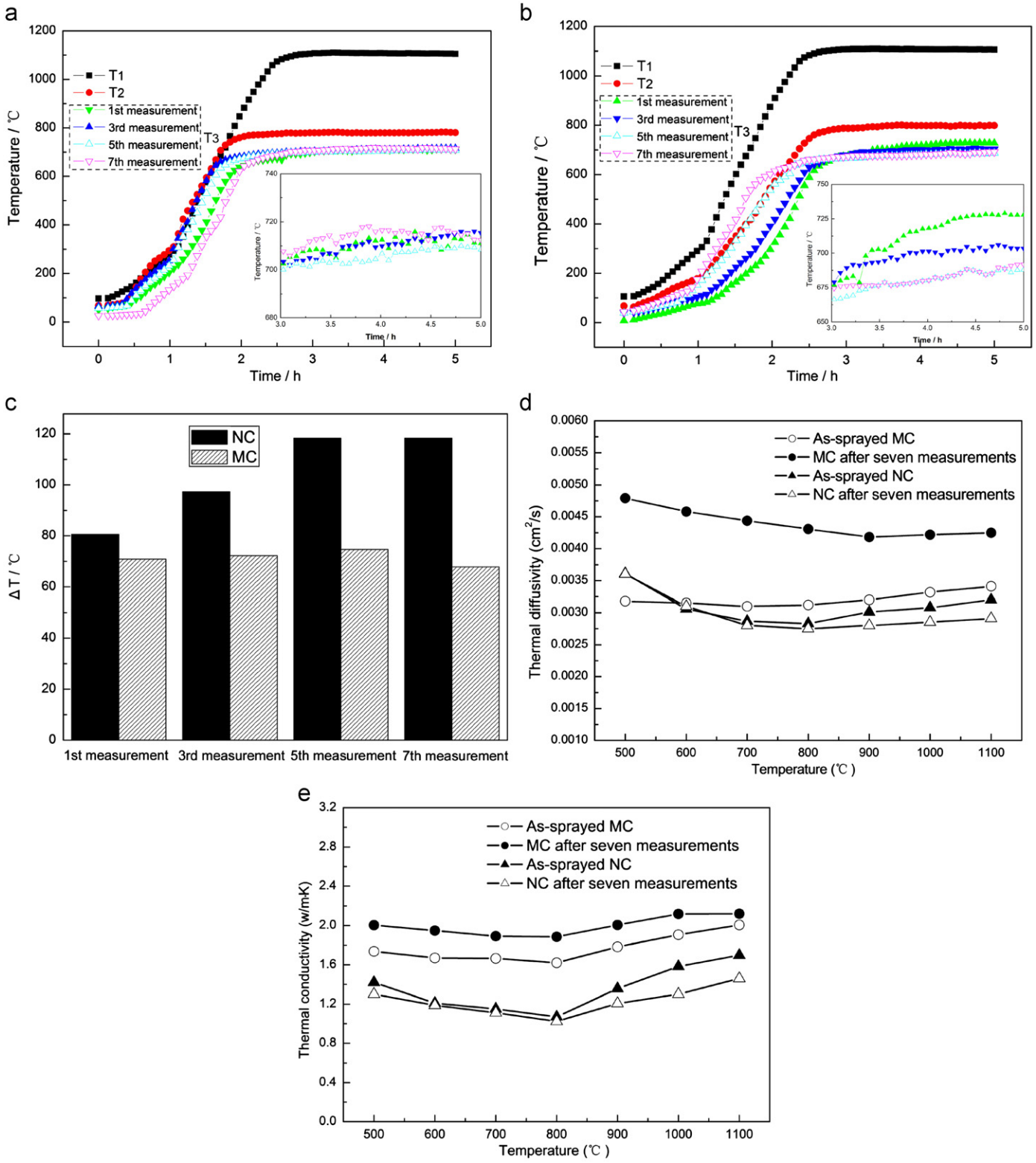

Fig. 8. Heating temperature curves of furnace (T_1), reference specimen backside (T_2) and TBCs specimen backside (T_3) after different test times: (a) MC, (b) NC, (c) comparison of ΔT between MC and NC, (d) variation in thermal diffusivity with temperatures and (e) variation in thermal conductivity with temperatures.

reduced to 68 °C during the seventh measurement, which was slightly lower than the as-sprayed coating. However, it was very interesting to find that the temperature drop of NC increased with increasing the testing times and reached to 118 °C during the seventh measurement. The mean value of seven measurements for NC and MC was

106 ± 14 °C and 69 ± 8 °C, indicating that the NC showed a better thermal insulation performance compared with MC. The variation in thermal diffusivity and thermal conductivity of the MC and NC from 500 °C to 1100 °C is plotted in Fig. 8d and e. As shown in Fig. 8d and e, the thermal diffusivity and thermal conductivity of the as-sprayed MC were 0.0031–0.0034 cm^2/s and 1.6–2.0 W/mK, whereas the thermal diffusivity and thermal conductivity of the as-sprayed NC were 0.0028–0.0036 cm^2/s and 1.0–1.7 W/mK, respectively. The reason for the decreased thermal conductivity in nanostructured coating has been widely reported, which are mainly associated with the phonon scattering as the result of the increased grain boundary [31,32]. In nanostructured coatings, the grains are smaller, and nanopores, micropores and inter-splat pores are present, which increase the number of interfaces, thereby enhancing phonon scattering, as a result, reducing the thermal conductivity. In addition, the thermal conductivity of as-sprayed NC was 1.4 W/mK at 500 °C, and it gradually decreased to 1.0 W/mK at 800 °C. Afterwards, the thermal conductivity increased with increasing the temperature and reached to 1.7 W/mK at 1100 °C due to the radiative heat which transfer took place through the material during the measurement of thermal conductivity at high temperatures [31,33]. The as-sprayed MC had a similar variation tendency with the NC in thermal conductivity with temperatures. After seven measurements, the thermal diffusivity and thermal conductivity of MC was significantly increased. Taking the thermal diffusivity and thermal conductivity at 800 °C as an example, the thermal diffusivity and thermal conductivity of coating after seven measurements were 0.0043 cm^2/s and 1.9 W/mK, increased by 39% and 19% than those of as-sprayed coating. However, for NC, the thermal diffusivity and thermal conductivity of coating were reduced to some extent after seven measurements, especially when the temperature was higher than 800 °C.

The temperature drop passing through the TBC system was calculated by one-dimensional heat transfer model under the steady-state heating condition. Fig. 9 shows the equivalent thermal circuits of TBC system involving some series and parallel thermal resistances due to layers of different materials. Therefore, the one-dimensional heat transfer rate for this system can be expressed as [34]:

$$q_x = \frac{T_1 - T_3}{\Sigma R_t} \tag{4}$$

where q_x is the heat transfer rate, T_1 is the temperature of furnace near the surface of TBC system measured by thermocouple 1, T_3 is the backside temperature of TBC system measured by thermocouple 3 and $\sum R_t$ is the summation of thermal resistance of each element. Because the platinum–rhodium thermocouple in the furnace was placed between an alumina tube and TBC system, the effect of tube wall on the temperature drop must be considered. Hence,

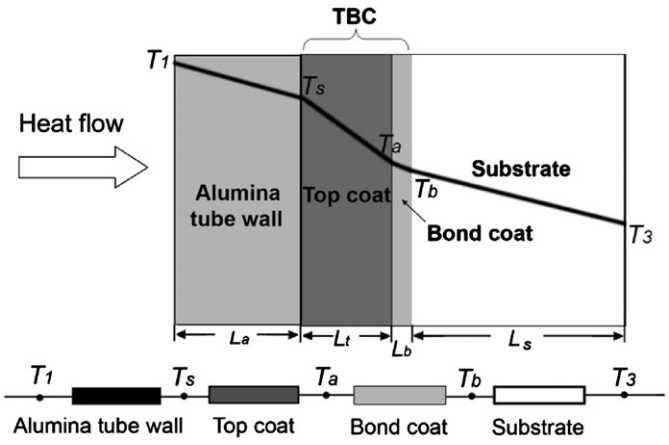

Fig. 9. Equivalent thermal circuit for one-dimensional heat transfer calculation.

$$q_x = \frac{T_1 - T_3}{[(L_a/k_aA) + (L_t/k_tA) + (L_b/k_bA) + (L_s/k_sA)]}$$

$$= \frac{T_s - T_b}{[(L_t/k_tA) + (L_b/k_bA)]} \tag{5}$$

$$\Delta T' = T_s - T_b = \frac{(T_1 - T_3)[(L_t/k_tA) + (L_b/k_bA)]}{[(L_a/k_aA) + (L_t/k_tA) + (L_b/k_bA) + (L_s/k_sA)]} \tag{6}$$

where L_a, L_t, L_b and L_s are thicknesses of alumina tube wall, YSZ top coat, metal bond coat and substrate, k_a, k_t, k_b and k_s are the thermal conductivities of alumina, YSZ top coat, metal bond coat and substrate respectively, A is the area, T_s, T_b and $\Delta T'$ are the surface temperature of TBC system in the furnace, the temperature at the interface between the bond coat and substrate and calculated temperature drop across TBC system respectively. Table 2 lists typical values of thickness and thermal conductivity of each element during the calculation. The experimental and calculated temperature drops across TBC system are shown in Table 3. As seen from Table 3, the calculated temperature drops had the same tendency with the experimental values. Meanwhile, the calculated ΔT was lower than the experimental value owing to the effect of the top coat/bond coat or bond coat/substrate interfacial thermal barrier resistance on the thermal conductivity of TBC system, which was not considered during the calculation of heat transfer process.

One can imagine that the thermal conductivity increased after several measurements due to the decrease of porosity or crack healing as the result of sintering at high temperatures, which also had a tendency to reduce or eliminate the effect of splat-interface resistance on conductivity. This can be explained the reason for the decreased temperature drop and increased thermal conductivity of MC after seven measurements. However, after one measurement, it was found that some fine cracks between the unmelted particles

Table 2
Typical values of thickness and thermal conductivity of each element during the one-dimensional heat transfer calculation.

	Alumina tube wall	Top coat	Bond coat	Substrate
Thickness (m)	2×10^{-3}	2×10^{-4}	6×10^{-5}	3.2×10^{-3}
Thermal conductivity ($W\,m^{-1}\,K^{-1}$)	5.8 (1400 K) [35]	1.4–2.1*	25.0 (1073 K) [36]	24.0 (1073 K) [36]

*According to the experimental values at 1100 °C (1373 K) as shown in Fig. 8d.

Table 3
Experimental and calculated temperature drops (ΔT) across TBC system.

Samples	Experimental ΔT (°C)	Calculated ΔT (°C)
As-sprayed MC	71	69
As-sprayed NC	81	76
MC after seven measurements	68	64
NC after seven measurements	118	101

and lamellar structures formed in the NC. The SEM micrograph of NC after one measurement is shown in Fig. 10. As seen from it, the unmelted nanoparticles in the as-sprayed coating rapidly grew during the test and the average grain size increased to about 1 μm. In addition, it was found that some fine cracks were formed between the unmelted particles and lamellar structures. These cracks were basically parallel to the top coat/bond coat interface and perpendicular to the direction of heat flow. Thus, they could effectively prevent the heat transfer through the coating, leading to the decrease of thermal conductivity and increase of temperature drop of NC. As stated in part I, the NC exhibited a multi-modal microstructure and the unmelted nanoparticles were loosely distributed between the lamellar structures. Due to the presence of porosity between the nanoparticles, they would be under a higher driving force for sintering and densification [37]. Therefore, the unmelted nanoparticles tended to densify or shrink at faster rates than those of lamellar structures, thereby leading to the formation of horizontal cracks between the unmelted nanoparticles and splats. It can be inferred from the above results that the sintering effect during the test was counteracted by the formation of the horizontal cracks in the NC, resulting in the improvement of thermal insulation performance.

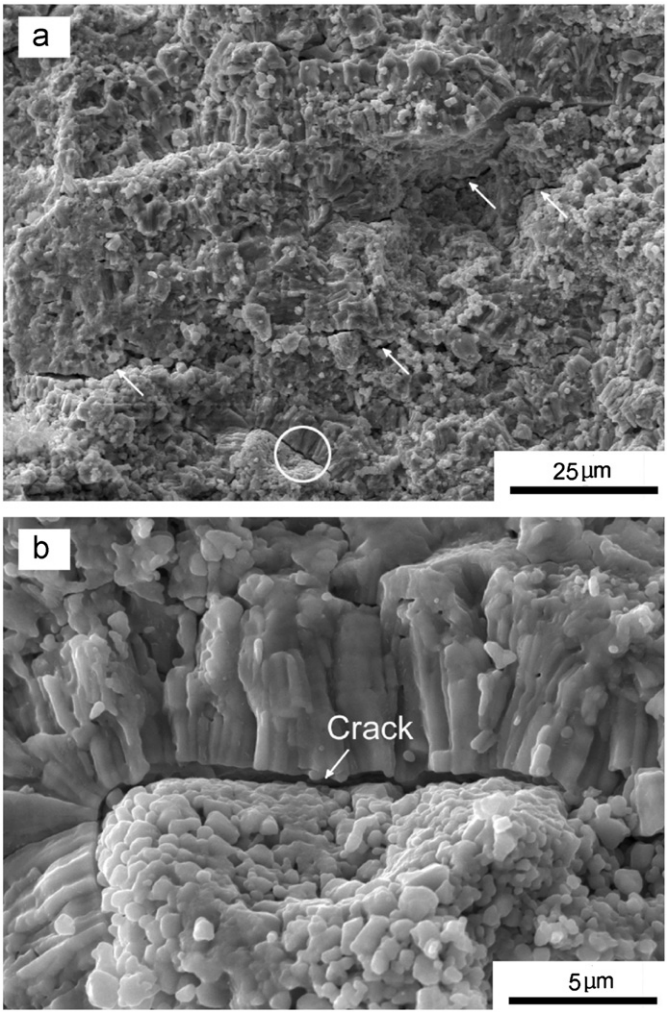

Fig. 10. SEM micrographs of NC after one measurement: (a) low-magnitude image where the microcracks were marked by white arrows, (b) a detailed view of the crack between the unmelted particles and lamellar structures in circular region of (a).

4. Outlook

Unlike the previously reported experimental results about the microstructure and property differences between the conventional microsized and nanostructured coatings, the microsized coating deposited by SAPS exhibited a denser microstructure and longer thermal cycling life. However, the multi-modal structure made nanostructured SAPS-coating showed a better thermal insulation performance compared with its microsized counterpart. Hence, as the second phase, the unmelted nanoparticles played a crucial role in the thermo-mechanical properties of nanostructured coating. For future research, the proportion of unmelted nano particles in the coating should be controlled reasonably by on-line monitoring the in-flight properties of particles in the plasma jet in order to tailor high-performance SAPS-coatings.

5. Conclusions

In this paper, the thermal shock resistance, oxidation resistance and thermal insulation performance of "conventional" microsized and nanostructured coatings (named as MC and NC respectively) deposited by supersonic

atmospheric plasma spraying (SAPS) were investigated. The conclusions are as follows:

1) Due to the improvement of intersplat cohesion and bonding strength between the top coat and bond coat, the MC presented a higher thermal shock resistance compared with NC.
2) The oxidation kinetics of both coatings followed a parabolic law. The weight gain of MC was slightly lower than that of NC before 600 h at 1100 °C. However, due to the formation of vertical cracks which penetrated the whole top coat, the weight gain for MC after 1000 h was slightly higher than that of NC, indicating the NC had a higher oxidation resistance after long time exposure.
3) NC showed a better thermal insulation performance compared with MC and the temperature drop (ΔT) of NC increased with the increase of testing times, because lots of fine cracks were formed between the unmelted particles and lamellar structures.

Acknowledgments

This work was supported by National Basic Research Program (Grant no. 2013CB035701), National Natural Science Foundation for Youth of China (Grant no. 51202187) and Research Fund of Key Laboratory for Advanced Technology in Environmental Protection of Jiangsu Province (Grant no. AE201006). The authors would like to thank Prof. B.J. Ding (Xi'an Jiaotong University, China) and technician Y.M. Qiang (Xi'an Jiaotong University, China) for their suggestions and help.

References

[1] A.G. Evans, D.R. Mumm, J.W. Hutchinson, G.H. Meier, F.S. Pettit, Mechanisms controlling the durability of thermal barrier coatings, Progress in Materials Science 46 (2001) 505–553.
[2] A.N. Khan, J. Lu, Behavior of air plasma sprayed thermal barrier coatings, subject to intense thermal cycling, Surface and Coatings Technology 166 (2003) 37–43.
[3] A.N. Khan, J. Lu, Thermal cyclic behavior of air plasma sprayed thermal barrier coatings sprayed on stainless steel substrates, Surface and Coatings Technology 201 (2007) 4653–4658.
[4] S. Widjaja, A.M. Limarga, T.H. Yip, Oxidation behavior of a plasma-sprayed functionally graded ZrO_2/Al_2O_3 thermal barrier coating, Materials and Letters 57 (2002) 628–634.
[5] B.A. Pint, I.G. Wright, W.Y. Lee, Y. Zhang, K. Prüßner, K.B. Alexander, Substrate and bond coat compositions: factors affecting alumina scale adhesion, Materials Science and Engineering A 245 (1998) 201–211.
[6] F.H. Yuan, Z.X. Chen, Z.W. Huang, Z.G. Wang, S.J. Zhu, Oxidation behavior of thermal barrier coatings with HVOF and detonation-sprayed NiCrAlY bondcoats, Corrosion Science 50 (2008) 1608–1617.
[7] A.C. Fox, T.W. Clyne, Oxygen transport by gas permeation through the zirconia layer in plasma sprayed thermal barrier coatings, Surface and Coatings Technology 184 (2004) 311–321.
[8] N.P. Padture, K.W. Schlichting, T. Bhatia, A. Ozturk, B. Cetegen, E.H. Jordan, M. Gell, S. Jiang, T.D. Xiao, P.R. Strutt, E. García, P. Miranzo, M.I. Osendi, Towards durable thermal barrier coatings with novel microstructures deposited by solution-precursor plasma spray, Acta Materialia 49 (2001) 2251–2257.
[9] Y. Bai, J.J. Tang, Y.M. Qu, S.Q. Ma, C.H. Ding, J.F. Yang, L. Yu, Z.H. Han, Submitted to Ceramics International, in press, http://dx.doi.org/10.1016/j.ceramint.2012.12.007.
[10] H. Chen, C.X. Ding, Nanostructured zirconia coating prepared by atmospheric plasma spraying, Surface and Coatings Technology 150 (2002) 31–36.
[11] B. Liang, C.X. Ding, Thermal shock resistances of nanostructured and conventional zirconia coatings deposited by atmospheric plasma spraying, Surface and Coatings Technology 197 (2005) 185–192.
[12] C.G. Zhou, N. Wang, Z.B. Wang, S.K. Gong, H.B. Xu, Thermal cycling life and thermal diffusivity of a plasma-sprayed nanostructured thermal barrier coating, Scripta Materialia 51 (2004) 945–948.
[13] R.S. Lima, A. Kucuk, C.C. Berndt, Bimodal distribution of mechanical properties on plasma sprayed nanostructured partially stabilized zirconia, Materials Science and Engineering A 327 (2002) 224–232.
[14] H.F. Liu, S.L. Li, Q.L. Li, Y.M. Li, W.X. Zhou, Microstructure, phase stability and thermal conductivity of plasma sprayed Yb_2O_3, Y_2O_3 co-stabilized ZrO_2 coatings, Solid State Sciences 13 (2011) 513–519.
[15] D.S. Almeida, C.R.M. Silva, M.C.A. Nono, C.A.A. Cairo, EB–PVD TBCs of zirconia co-doped with yttria and niobia, a microstructural investigation, Surface and Coatings Technology 200 (2006) 2827–2833.
[16] F. Cernuschi, P. Bianchi, M. Leoni, P. Scardi, Thermal diffusivity/microstructure relationship in Y-PSZ thermal barrier coatings, Journal of Thermal Spray Technology 8 (1999) 102–109.
[17] R.S. Lima, A. Kucuk, C.C. Berndt, Evaluation of microhardness and elastic modulus of thermally sprayed nanostructured zirconia coatings, Surface and Coatings Technology 135 (2001) 166–172.
[18] W.R. Chen, X. Wu, B.R. Marple, P.C. Patnaik, The growth and influence of thermally grown oxide in a thermal barrier coating, Surface and Coatings Technology 201 (2006) 1074–1079.
[19] T.J. Nijdam, G.H. Marijnissen, E. Vergeldt, A.B. Kloosterman, W.G. Sloof, Development of a pre-oxidation treatment to improve the adhesion between thermal barrier coatings and NiCoCrAlY bond coatings, Oxidation of Metals 66 (2006) 269–294.
[20] F. Cao, B. Tryon, C.J. Torbet, T.M. Pollock, Microstructural evolution and failure characteristics of a NiCoCrAlY bond coat in hot spot cyclic oxidation, Acta Materialia 57 (2009) 3885–3894.
[21] E.A.G. Shillington, D.R. Clarke, Spalling failure of a thermal barrier coating associated with aluminum depletion in the bond-coat, Acta Materialia 47 (1999) 1297–1305.
[22] R.S. Lima, B.R. Marple, Thermal spray coatings engineered from nanostructured ceramic agglomerated powders for structural, thermal barrier and biomedical applications: a review, Journal of Thermal Spray Technology 16 (2007) 40–63.
[23] M. Gell, E. Jordan, K Vaidyanathan, K. McCarron, B. Barber, Y.H. Sohn, V.K. Tolpygo, Bond strength, bond stress and spallation mechanisms of thermal barrier coatings, Surface and Coatings Technology 120–121 (1999) 53–60.
[24] Q.H. Yu, A. Rauf, N. Wang, C.G. Zhou, Thermal properties of plasma-sprayed thermal barrier coating with bimodal structure, Ceramics International 37 (2011) 1093–1099.
[25] Z.M. Li, S.Q. Qian, W. Wang, J.H. Liu, Microstructure and oxidation resistance of magnetron-sputtered nanocrystalline NiCoCrAlY coatings on nickel-based superalloy, Journal of Alloys and Compounds 505 (2010) 675–679.
[26] L. Ajdelsztajn, J.A. Picas, G.E. Kim, F.L. Bastian, J. Schoenung, V. Provenzano, Oxidation behavior of HVOF sprayed nanocrystalline NiCrAlY powder, Materials Science and Engineering A 338 (2002) 33–43.
[27] G.D. Girolamo, F. Marra, C. Blasi, E. Serra, T. Valente, Microstructure, mechanical properties and thermal shock resistance of

plasma sprayed nanostructured zirconia coatings, Ceramics International 37 (2011) 2711–2717.
[28] C.H. Lee, H.K. Kim, H.S. Choi, H.S. Ahn, Phase transformation and bond coat oxidation behavior of plasma-sprayed zirconia thermal barrier coating, Surface and Coatings Technology 124 (2000) 1–12.
[29] T. Jessen, E. Ustundag, in: Proceedings of the 24th Annual Conference on Composites, Advanced, Ceramics, Materials, and Structures: B, 2000, The American Ceramic Society, Westerville, OH, USA.
[30] Y. Liu, C. Persson, J. Wigren, Experimental and numerical life prediction of thermally cycled thermal barrier coatings, Journal of Thermal Spray Technology 13 (2004) 415–424.
[31] A. Rauf, Q. Yu, L. Jin, C. Zhou, Microstructure and thermal properties of nanostructured lanthana-doped yttria-stabilized zirconia thermal barrier coatings by air plasma spraying, Scripta Materialia 66 (2012) 109–112.
[32] H. Zhou, F. Li, J. Wang, B.D. Sun, Microstructure analyses and thermophysical properties of nanostructured thermal barrier coatings, Journal of Coatings Technology and Research 6 (2009) 383–390.
[33] D.R. Clarke, Materials selection guidelines for low thermal conductivity thermal barrier coatings, Surface and Coatings Technology 163–164 (2003) 67–74.
[34] F.P. Incropera, D.P. Dewitt, Introduction to Heat Transfer, John Wiley & Sons, Inc., New York, USA, 1985, PP. 66-67.
[35] X.Q. Cao, R. Vassen, D. Stoever, Ceramic materials for thermal barrier coatings, Journal of European Ceramic . Society 24 (2004) 1–10.
[36] D.M. Zhu, R.A. Miller, Thermal conductivity and elastic modulus evolution of thermal barrier coatings under high heat flux conditions, Journal of Thermal Spray Technology 9 (2000) 175–180.
[37] R.S. Lima, B.R. Marple, Nanostructured YSZ thermal barrier coatings engineered to counteract sintering effects, Materials Science and Engineering A 485 (2008) 182–193.